Photocatalytic activation of Ag-doped SrSnO$_3$ nanorods under visible light for reduction of p-nitrophenol and methylene blue mineralization

Z. Ghubish[1], R. Kamal[2], Hala R. Mahmoud[1], M. Saif[2], H. Hafez[3], and M. El-Kemary[1,*]

[1] *Institute of Nanoscience & Nanotechnology, Kafrelsheikh University, Kafr El-Sheikh 33516, Egypt*
[2] *Chemistry Department, Faculty of Education, Ain Shams University, Roxy, Cairo 11711, Egypt*
[3] *Natural Resources Department, Environmental Studies and Research Institute, University of Sadat City, Sadat City, Egypt*

ABSTRACT

The utilization of solar energy for the treatment of wastewater pollutants by photocatalysts has been considered a promising solution to address environmental problems. Herein, we have synthesized silver nanoparticle-doped strontium stannate (Ag-doped SrSnO$_3$) nanorods by hydrothermal method followed by ultrasonic treatment. The developed nanocomposites were applied for photocatalytic reduction of p-nitrophenol (4-NP) and methylene blue (MB) mineralization under visible light illumination. The effect of hydrothermal duration time (16–25) h, Cetyltrimethylammonium bromide (CTAB) and silver nanoparticles (Ag NPs) concentration (0.5–2.5) wt% on the crystal, surface, optical, photoluminescence as well as photocatalytic activity were studied. A well-defined crystalline cubic phase of SrSnO$_3$ was obtained. CTAB inhibits the crystal growth of SrSnO$_3$. Reduction of 4-NP and MB mineralization were used as two-model reactions for testing the effect of Ag doping concentration on the photocatalytic activities of Ag/SrSnO$_3$ under visible light illumination. The obtained results show that 2.0 wt% of Ag-doped SrSnO$_3$ exhibits efficient photocatalytic reduction of 4-NP with 98.2% conversion within 5 min of reaction time. Also, 87% of the MB sample was mineralized after 1 h of visible illumination using 2.0% Ag/SrSnO$_3$ in the presence of H$_2$O$_2$. Besides, we have discussed the possible photocatalytic mechanism for reduction of 4-NP and mineralization of MB using 2.0 wt% of Ag doped SrSnO$_3$ under visible light illumination.

Address correspondence to E-mail: elkemary@nano.kfs.edu.eg; elkemary@yahoo.com

1 Introduction

Environmental pollution is one of the main global challenges of the twenty-first century. Among the various resources for environmental pollution, water pollution is regarded as one of the most negative effects for the mankind and ecosystem [1, 2]. Industrial, domestic, and agricultural activities and other environmental and global changes are the main water pollution sources, which may cause serious health problems to humans [3]. Wastewater treatment and reuse for beneficial purposes is an essential requirement for a healthy lifestyle, environmental sustainability, and social equity.

Several methods have been developed for wastewater treatment. Photocatalytic degradation of pollutants is a promising technology for the efficient wastewater treatment. It is comparatively inexpensive, simple, and environment friendly [4–6]. In the past 30 years, various photocatalysts have been reported. Among of them, alkaline earth perovskite stannate ($MSnO_3$, M = Ca^{2+}, Sr^{2+}, Ba^{2+}) were used as photocatalyst in recent years [7]. Perovskite $SrSnO_3$ is semiconductor with wide bandgap energy ($\sim$3.8–4.2 eV) [8]. Under UV illumination, its charge carriers are easily separated. These separated charge carriers are responsible for photocatalytic activity of $SrSnO_3$. The wide bandgap energy is the main disadvantages of $SrSnO_3$ photocatalyst. As consequences, $SrSnO_3$ absorbs UV light only from the solar spectrum. Another disadvantage of $SrSnO_3$ as a photocatalyst is high charge carriers' recombination rate [9, 10].

Overcoming these challenges requires the doping of metal NPs onto perovskite. Manganese doping in $CsPbCl_3$ Nanocrystalline drastically enhances their optical properties due to the charge transfer of photoinduced excitons from the $CsPbCl_3$ host to the dopant Mn^{2+} centers [11]. Noble transition metals such as Ag NPs and their composites with semiconducting oxide have attracted increasing attention because they could induce Surface Plasmonic Resonance (SPR). The SPR was used to assist the efficiency of photocatalyst in the visible absorption range. When noble metal nanoparticles are deposited on the surface of a semiconductor, they display unique optical and catalytic capabilities that are not seen in bulk metal due to transferring photoexcited electrons from the Ag NPs to TiO_2 Conduction Band (CB), which facilitate charge separation. Gerisher has

emphasized the importance of dioxygen reduction by CB electrons, which avoids the recombination of photogenerated charge carriers. Therefore, superoxide radical production could be the slowest stage in the reaction sequence leading to substrate oxidation [12, 13]

Although a wide range of alkaline earth stannate $MSnO_3$ (M = Sr, Ca, Ba) compounds have been synthesized and studied from a structural, magnetic, and electrical, photoluminescence, theoretical point of view [14], only a few have been attempted in studding the photocatalytic activity of pure and doped $SrSnO_3$ nanoparticles. For instance, Jun ploy et al. [15] applied Ag-doped $SrSnO_3$ composites for Methylene blue degradation under ultraviolet Radiation. Venkatesh et al. [16] prepared rGO- $SrSnO_3$ nanocomposites for degradation of aqueous methylene blue dye under UV light irradiation. The $SrSnO_3$/g-C_3N_4 was synthesized by a facile solid-state method and applied to visible light-mediated photocatalysis in both, wet and dry phase [17]. Subhan et al. [14] synthesized triple metal oxide from Ag/$SrSnO_3$ by a co-precipitation method for dye removal, antibacterial and sensing applications. However, no attempts of preparing Ag/$SrSnO_3$ by hybrid hydrothermal/ultrasonic method for p-nitrophenol (4-NP) reduction and methylene blue (MB) mineralization under visible light illumination can be found among literature data.

In this report, we have focused on preparation of an efficient Ag-doped $SrSnO_3$ photocatalyst for degradation of common environmental pollutants in daily life as methylene blue (MB) dye and 4-nitrophenol (4-NP) under visible light illumination, and to evaluate the catalytic performance of the developed catalyst.

2 Materials and methods

2.1 Material

Strontium nitrate ($SrNO_3$), Tin (IV) chloride pentahydrate, silver nitrate ($AgNO_3$), 4-nitrophenol (4-NP) and methylene blue (MB) were obtained from Sigma-Aldrich. Cetyltrimethylammonium bromide (CTAB) was purchased from Belami fine chemical. Sodium hydroxide (NaOH) and hydrochloric acid (HCl) were obtained from Germany Company. All

materials used were of analytical grade and were used without further purification.

2.2 Preparation SrSnO₃ nanorods

$Sr(NO_3)_2$ (10 mmol), $SnCl_4 \cdot 5H_2O$ (10 mmol), CTAB (1.5 mmol) and H_2O (30 mL) were mixed together under continues stirring. Add 1 mol/L NaOH until the pH of the solution adjusted to 13, white suspension was obtained. Then, the suspension was transferred into a Teflon-lined stainless autoclave with about 80% degree of fill. The sealed vessel was then heated at 160 oC for $\sim$ 18 h, and then cooled to room temperature. The obtained precipitate was filtered and washed for several times with distilled water. The obtained powder was calcinated at 700 °C for 3 h [15].

2.3 Preparation Ag and Ag doped SrSnO₃

To synthesize silver nanoparticle-doped strontium stannate nanorod (Ag/SrSnO₃), $AgNO_3$ (0.5–2.5 wt%) was mixed with 1 g SrSnO₃ and 50 mL of ethylene glycol (EG, $C_2H_6O_2$) under magnetic stirring. The mixture was ultrasonically vibrated for 15 min to form dispersed and de-agglomerated brown suspension. Then the product was separated, washed several times with absolute ethanol, and dried in air at 70 °C for 24 h [15]. Pure silver nanoparticles (Ag NP-1) were also prepared using the similar procedure using1 mmol of silver nitrate and 50 mL of ethylene glycol (EG, $C_2H_6O_2$). Brown product was separated by centrifugation at 12,000 rpm and washed three times by distilled water. The produced silver nanoparticles (Ag NP-2) from 2 mL of 0.001 M silver nitrate were added drop wise to 30 mL of 0.002 M sodium borohydride solution that had been chilled in an ice bath. The reaction mixture was stirred vigorously till the solution turned to pale yellow [18].

2.4 Photocatalytic reduction of 4-NP

40 µL of 4-NP (0.01 M) was added to 2.8 mL deionized water and then mixed with 80 µL of freshly prepared $NaBH_4$ (0.5 M). After that, 5 mg of Ag/SrSnO₃ photocatalyst (0.0–2.5 wt%) was added to the above solution with stirring for 30 min to reach the adsorption/desorption equilibrium. The reaction mixture was illuminated using halogen lamp (500 W;

$\lambda > 420$ nm). The above procedures were repeated under dark condition in the presence of 0.0–0.5 wt% Ag/SrSnO₃. Moreover, blank experiments were done in the presence of $NaBH_4$ only under dark and light condition.

2.5 Photocatalytic degradation of MB

20 mg of photocatalyst (0.0–2.5) weight percent (wt%) Ag/SrSnO₃ was added to an aqueous solution of MB (in 25 mL; 10 ppm). The reaction mixture was stirred in the dark for 30 min to reach the adsorption/desorption equilibrium. Then H_2O_2 (0.08 M) was added. Then, the halogen lamp was turned on to start the photoreaction. The decolorization of MB was followed using UV–Vis. Spectrophotometer. Also, the mineralization of MB was followed up using total organic carbon technique (TOC). The same experiment was done at three different pH values (3.0, 6.0, 11) in the presence of 2.0 wt% of Ag/SrSnO₃ under visible light illumination. A series of blank experiments for MB in the presence of H_2O_2, SrSnO₃ and 0.5 wt% Ag/SrSnO₃ in the dark were tested.

## 2.6 Characterization of the photocatalysts

The crystalline and phase structure of the materials were performed using Shimadzu 6000 X-ray diffractometer (XRD) (Cu-K radiation = 1.5406 Å) as reported in detail elsewhere [19]. The morphology of the synthesized nanostructured were investigated by Transmission electron microscope (TEM) (200 kV, JEOL-JEM-2100, Tokyo, Japan) and scanning electron microscope (SEM) (FEI Sirion) equipped with an Energy Dispersive X-Ray (EDX) detector (S-3400 N II, Hitachi, Japan). Shimadzu UV-2450 spectrophotometer was used to measure the diffuse reflectance spectrum (UV–Vis DRS) using $BaSO_4$ as a reference sample. The photoluminescence (PL) spectra were characterized with (Shimadzu RF-5301PC) spectrofluorometer. Thermogravimetric analysis (TGA-50) and Differential thermal analysis (DTA-50) was tested in the range from 50 to 800 with Shimadzu thermogravimetric analyzer at a constant heating rate (10 min or 1) in nitrogen gas. Fourier-transform infrared spectroscopy (FTIR) was measured with KBr disks using JASCO FTIR-6800.

3 Results and discussion

3.1 XRD

The effect of hydrothermal time at 160 °C on the crystal structure of as-synthesized $SrSnO_3$ in the absence and presence of CTAB was studied by XRD analysis. The XRD patterns are shown in Fig. 1a (I). The observed diffraction peaks of hexagonal phase $SrSn(OH)_6$ matched well with precursor (JCPDS-ICDD card No.090086) [20]. However, up on hydrothermal treatment at 160 °C for different duration times in absence and presence of CTAB, a well-defined crystalline cubic phase of $SrSnO_3$ was obtained (JCPDS-ICDD card No. 22–1442) [21], Fig. 1a (II–VII). The diffraction peaks located at 21.54, 30.8, 44.47, 55.66, 64.96, 73.86 are related to (200), (202), (400), (440), (442), (620) crystallographic planes. The observed data of the prepared photocatalysts are summarized in Table 1. In the absence of CTAB, as

the hydrothermal duration increase the full width at half maximum (FWHM) of $SrSnO_3$ decreases (Table 1). In addition, an increase in the lattice parameter values was observed, reflecting that heat treatment can appreciably influence $SrSnO_3$ crystallinity. However, on the presence of CTAB, $SrSnO_3$ exhibited a reverse behavior suggesting that the presence of CTAB during preparation inhibits the crystallization of $SrSnO_3$. Figure 1b shows the XRD pattern of $SrSnO_3$ at different Ag loading content wt%. The results XRD spectral pattern exhibited XRD peaks belonging to $SrSnO_3$, in addition to a minor phase of Ag NPs ($2\theta = 38.12°$ and $44.2°$) was observed at higher concentrations of Ag NPs (2.0 and 2.5 wt%) (JCPDS Card 04–0783), Fig. 1c shows XRD patterns of pure Ag NP-1and Ag NP-2 [22]. Doping of Ag NPs on the surface of $SrSnO_3$ may be due to the reduction Ag^+ by EG during ultra-sonication step. As Ag NPs concentration increase, the intensity of the main diffraction peak of $Ag/SrSnO_3$ at (202) was
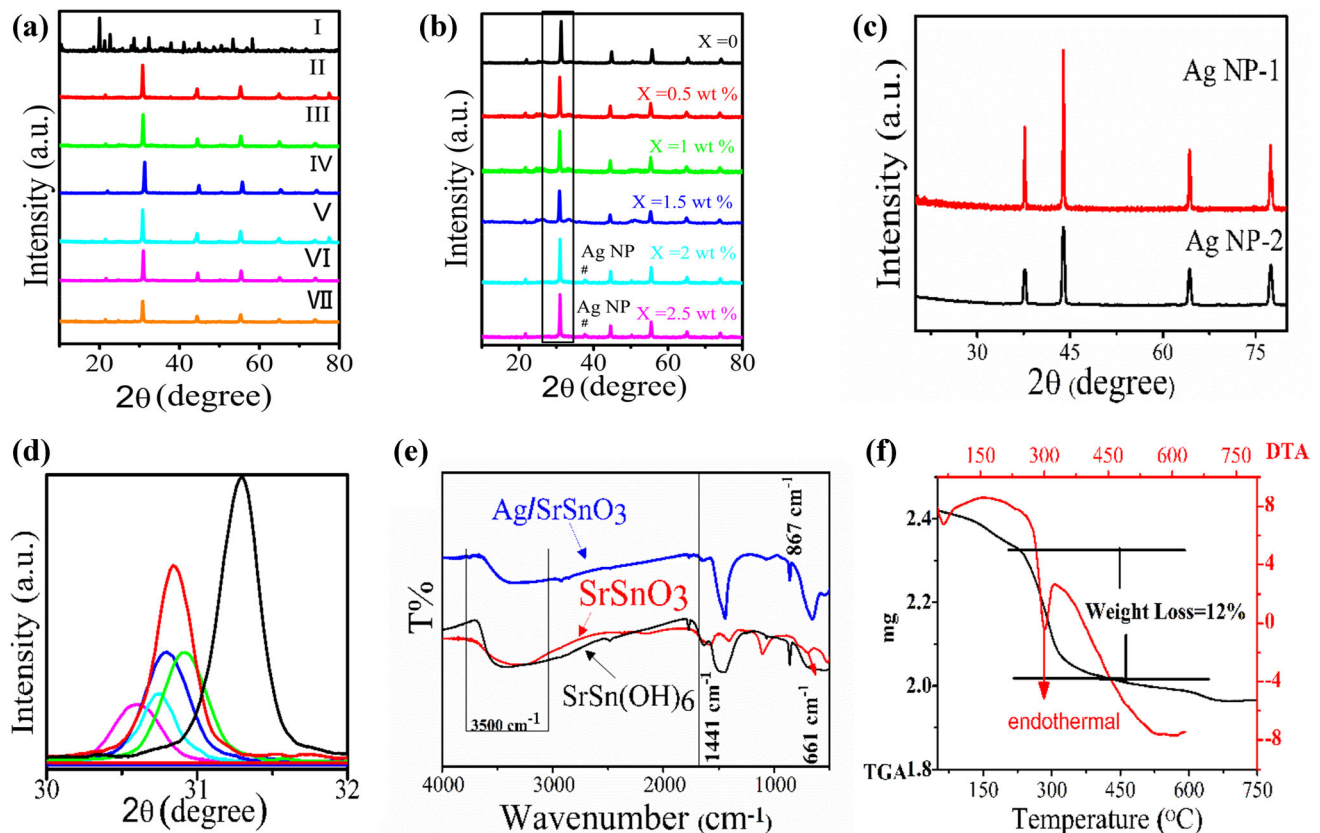
Fig. 1 a XRD patterns of $SrSn(OH)_6$ precursor (I); $SrSnO_3$ hydrothermally treated at 16, 20,25 h (II, III, IV) without CTAB; and in the presence of CTAB at 16, 20, 25 h (V, VI, VII) respectively. XRD patterns (**b, d**) of 0–2.5 wt% of $Ag/SrSnO_3$ 25 h in the presence of CTAB(B), **c** XRD patterns of Ag NP-1, Ag NP-2 (**e**) FT-IR spectra of $SrSn(OH)_6$, $SrSnO_3$, $Ag/SrSnO_3$ and **f** TGA/DTA patterns of the precursor $SrSn(OH)_6$.

Table 1 Crystal parameters of $SrSnO_3$ nanoparticle at different preparation conditions in the absence and presence of CTAB

Conditions	Reaction time/h	2θ (°)	Lattice parameter	FWHW (202)
Without CTAB	16	30.90	8.0315	0.2735
	20	30.79	8.1729	0.2725
	25	30.87	8.2012	0.2660
With CTAB	16	31.27	8.1163	0.2765
	20	30.57	8.1050	0.2816
	25	31.30	8.1060	0.2885

gradually decreased. This phenomenon is likely due to Ag NPs can inhibit the growth of $SrSnO_3$ crystal (Table 2). In addition, it was observed that the main diffraction peak was shifted to lower angle as a function of Ag NPs concentration. Also, it is observed that the lattice parameter decreased by increasing Ag NPs loading content in the Ag/$SrSnO_3$, Fig. 1d. This is due to growing of small size of Ag NPs (10–40 nm) on the surface of micro scale $SrSnO_3$ rods, which minimize the total surface energy of Ag/$SrSnO_3$ system.

Figure 1e shows the FTIR spectrum of the $SrSn(OH)_6$ precursor, $SrSnO_3$ and 2 wt% Ag NPs-doped $SrSnO_3$ NPs. $SrSn(OH)_6$ exhibits peak at 850 cm^{-1} due to bending mode of the hydroxyl group. This peak disappears after formation of $SrSnO_3$ NPs. $SrSn(OH)_6$ shows broad peaks at 3500 and 1441 cm^{-1} due to adsorbed water molecules [22]. However, $SrSnO_3$ and 2 wt% Ag/$SrSnO_3$ exhibit peak in the range of $521–660 \text{ cm}^{-1}$ which is attributed to vibration of the O–Sn–O bridging [23]. The FTIR spectrum of 2 wt% Ag/$SrSnO_3$ nanocomposite shows small shift in the absorption peaks, due to the charge transfer interaction between Ag NPs and oxygen atoms in the $SrSnO_3$ NPs. Furthermore, the peak intensity at 1440 cm^{-1} was increased due to presence of the OH groups on the surface. Therefore, Ag NPs attached on the surface of $SrSnO_3$ can improve its surface state and generate more hydroxyl groups on the surface.

The TG-DTA analysis were performed to determine the temperature and weight change for decomposition of the precursor $SrSn(OH)_6$ into $SrSnO_3$ phase. Figure 1f displays the TGA thermogram with three different steps, which showed $\sim$ 18% total weight loss on the temperature range 25–800 °C. The first step from 25 to 200 °C with the weight loss $\sim$ 3.5% due to the evaporation of water and ethanol physically adsorbed on surfaces of the precursors. At 200–350 °C, the faster weight loss (12%) corresponding to the dehydration and dihydroxylation processes of the Sr–Sn–O–H precursor. The third step 530–800 °C showed complete release of H_2O molecules from their grains, with the formation of $SrSnO_3$. The observed phase change of $SrSn(OH)_6$ precursors into $SrSnO_3$ at 700 °C via three endothermic peaks (37, 275, 563 °C) in the DTA thermogram shows similar behavior throughout the decomposition process to produce $SrSnO_3$ [24].

Figure 2 shows SEM images of $SrSnO_3$ at different hydrothermal times in the absence and presence of CTAB. In the absence of CTAB, the irregular shape from $SrSnO_3$ converted to rod-like shape by increasing hydrothermal time, Fig. 2a–c. The average diameter and length of rods are 700 μm and 5 μm, respectively. Presence of CTAB during preparation allows the formation of rod shape at different hydrothermal duration times, Fig. 2d–f. The rod diameter decreases from 1–2 μm to 200–300 nm as hydrothermal time are increased from 16 to 25 h at same CTAB concentration. The rod length is also

Table 2 The crystal parameters of $SrSnO_3$ at different wt% content of Ag NPs ($SrSnO_3$ prepared by hydrothermal method at 160 °C for 25 h in the presence of CTAB)

Ag wt%	2θ (°)	Lattice parameter, a (nm)	FWHW (202)	Band ap (eV)
0.0	31.30	8.1060	0.2885	3.80
0.5	30.82	8.0889	0.2886	3.71
1.0	30.86	8.0888	0.2889	3.63
1.5	30.78	8.0680	0.2912	3.60
2.0	30.70	8.0428	0.2923	3.53
2.5	30.50	8.0315	0.2963	3.52

reduced by addition of CTAB. Additionally, CTAB and hydrothermal reaction time have significant effect on the morphology and size of the $SrSnO_3$.

No changes in the morphology of $SnSrO_3$ after Ag NPs loading are observed, Fig. 2g–i. SEM and TEM showed the uniform loading of Ag NPs on the surface of $SnSrO_3$. Nevertheless, some Ag NPs has little aggregation on the surface. The SEM–EDS spectrum of $Ag/SrSnO_3$, Fig. 2j displays the presence of Sr, Sn, O and Ag elements.

Figure 3a depicts the UV–Visible (UV–Vis) absorption spectra of $SrSnO_3$ on the absence and presence of different concentrations of Ag NPs. As shown on Fig. 3a, $SrSnO_3$ shows a broad absorption band at 285 nm due to intrinsic exciton absorption, [25, 26]. $Ag/SrSnO_3$ rod shows an additional absorption band in the visible region (427 nm), Fig. 3a. The intensity of this band increases by increasing the content of Ag NPs loading, which is due to the characteristic plasmon surface resonance (SPR) phenomenon of free electron in Ag NPs conduction bands [27, 28]. This confirms the presence of Ag NPs on the surface of SrSnO3, as shown in Fig. 3b.
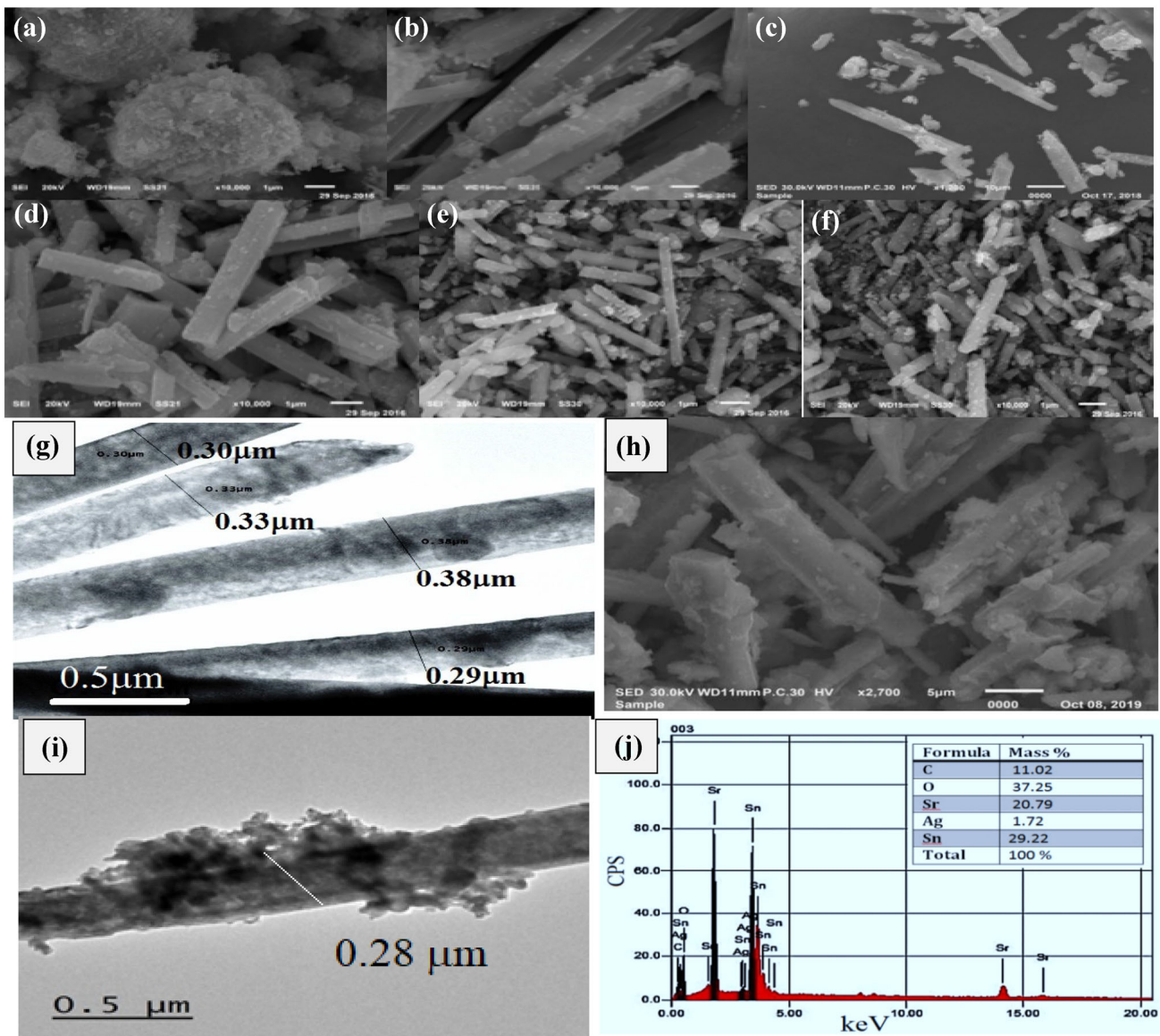
Fig. 2 SEM images of $SrSnO_3$ at hydrothermally treated at 16, 20, 25 h (a, b, c) without CTAB; and in the presence of CTAB at 16, 20, 25 h (d, e, f), respectively, scale bar 1 μm. TEM images g of $SnSrO_3$ nanorod, The SEM and TEM images h, i of 2 wt% Ag/$SnSrO_3$ Nanorods, and j EDX of 2 wt% Ag/$SnSrO_3$ Nanorods
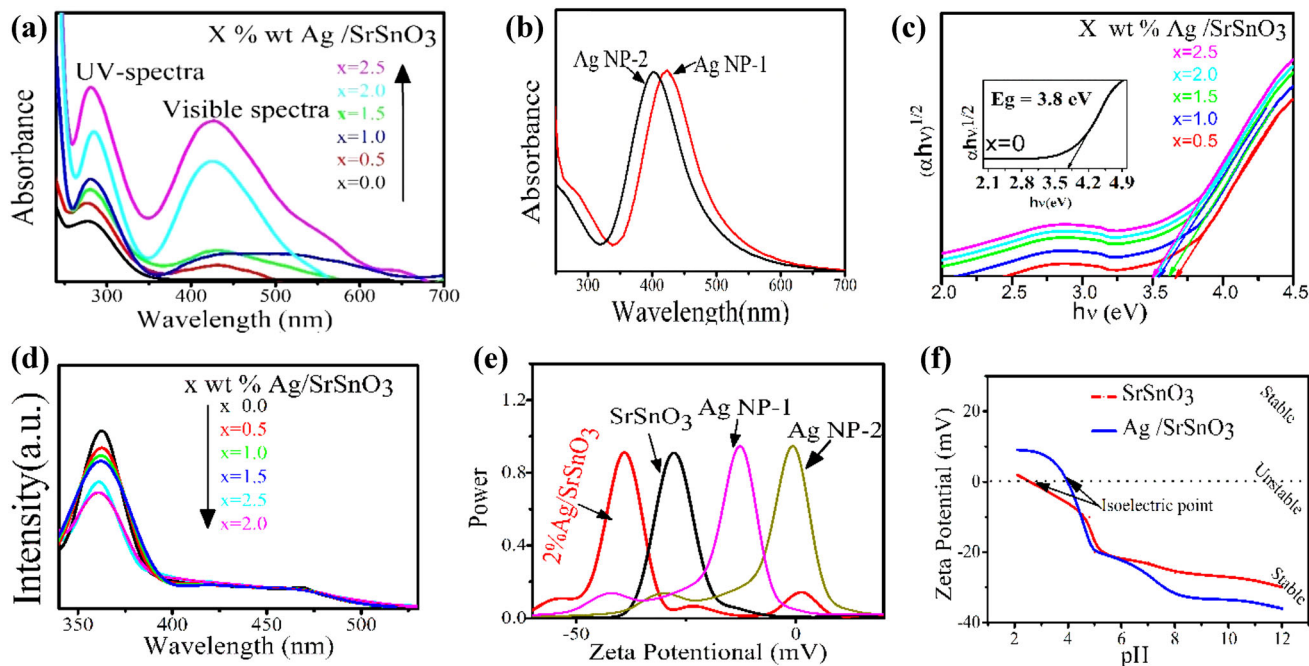
Fig. 3 Effect of Ag NPs concentration on the UV–Vis absorption of Ag/SrSnO₃ (a) UV–Vis absorption of Ag NP (b). Plot of $(\alpha h \upsilon)^{1/2}$ versus photon energy of Ag/SrSnO₃ c, PL spectra of Ag/SrSnO₃ (d), Zeta potential measurements of the samples (e) and effect of pH on the Zeta potential of SrSnO₃ and 2 wt% Ag/SrSnO₃

The bandgap energy values of Ag/SrSnO₃ at different Ag NPs loading concentrations were determined using the following Wood and Tauc Eq. (1) [29]:

$$\alpha h \upsilon = C(h \upsilon - E_g)^n \quad (1)$$

where α is the absorbance, $h\upsilon$ is the photon energy and C is a band tailoring constant. The nature of the optical transition in the semiconductor is indicated by the exponent "n". The values of n are 2 and ½ for allowed indirect and direct optical transitions, respectively [30]. Plotting $(\alpha h \upsilon)^{1/2}$ versus $h\upsilon$ according to relationship (1) leads to the evaluation of the bandgap energy (E_g) by extracting the linear portion of curves to $(\alpha h \upsilon)^{1/2} = 0$, Fig. 3c. The calculated bandgap energy values of Ag/SrSnO₃ NPs are summarized in Table 2. As can be seen from Table 2, values of E_g decrease with increasing content of Ag loading, and the observed E_g values are relatively lower than some reported literature values (4.1–3.9 eV) [31]. Figure 3c show a high absorption peak at 2.9 eV, which is ascribed to the surface deposition of Ag NPs.

Figure 3d shows the photoluminescence (PL) emission spectra of SrSnO₃ at different Ag NPs concentrations ($\lambda_{ex} = 275$ nm). Notably, the PL emission

of SrSnO₃ results from indirect transition of the excited electron from the conduction band to valance band. However, the PL of Ag/SrSnO₃ rods were quenched as Ag loading increased. This quenching is because the doped Ag NPs on the surface of SrSnO₃ acts as electron trapping under UV excitation, in which, Ag NPs can trap the SrSnO₃ excited electrons on the conduction band. We assume that Ag NPs retard the electron–hole recombination in the SrSnO₃ rods, which, increases the photocatalytic efficiency of the Ag/SrSnO₃ under UV excitation [32].

The observed ς-potential values (Fig. 3e) of SrSnO₃, Ag/SrSnO₃, Ag NP-1 and Ag NP-2 suspension in water are − 27.4 Mv, − 39 mV, − 15 mV and 0 mV, respectively. These high negative charges suggesting the electrical stability of the Ag/SrSnO₃ is higher than that of SrSnO₃ and Ag NP 1–2, i.e., resist aggregation. [33, 34].The effect of pH on the zeta potential of SrSnO₃ and Ag/SrSnO₃ rods on the pH range 1–12 is shown in Fig. 3e. The estimated isoelectric points of SrSnO₃ and optimized Ag/SrSnO₃ are at pH values of 3.8 and 4.2, respectively. The observed negative zeta potential values suggesting enhanced adsorption of MB (cationic dye) on the surface of photocatalyst at these pH values [35]. This is because the photo-generated holes after irradiation

and excitation of electrons from the valence to the conduction band either directly oxidize the dye to reactive intermediates or react with hydroxyl ions (OH$^-$) leading to the formation of highly oxidative hydroxyl radicals (OH$^{\cdot}$) and further complete the degradation of the dye.

3.2 Photocatalytic applications

3.2.1 Photocatalytic reduction of 4-nitrophenol

Figure 4a, b show effect of NaBH$_4$ on 4-NP in dark and visible light illumination was tested. Also, the photocatalytic activity of SrSnO$_3$ on 4-NP was performed in dark and visible light illumination as

shown in Fig. 4c, d. The obtained results show a very small change in the absorption spectrum of 4-NP in the presence of only SrSnO$_3$ or NaBH$_4$. In all experiments, the adsorption/desorption equilibrium was performed by adding 5 mg of photocatalyst to 4-NP under stirring for 30 min in dark. as shown in Fig. 4e, weak adsorption of 4-NP was observed on the photocatalyst surface. As shown in Fig. 4, the absorption spectrum of 4-NP changed insignificantly in the presence of only Ag NP (1, 2) in the dark (f, g). However, in the presence of Ag NP (1, 2) and NaBH$_4$, a small change in the absorption spectrum of 4-NP was observed under visible light. This is because the negative charges of Ag NP-1 (− 12 mV) and Ag-2 (− 2 mV) adsorbed weakly with the negative charge of
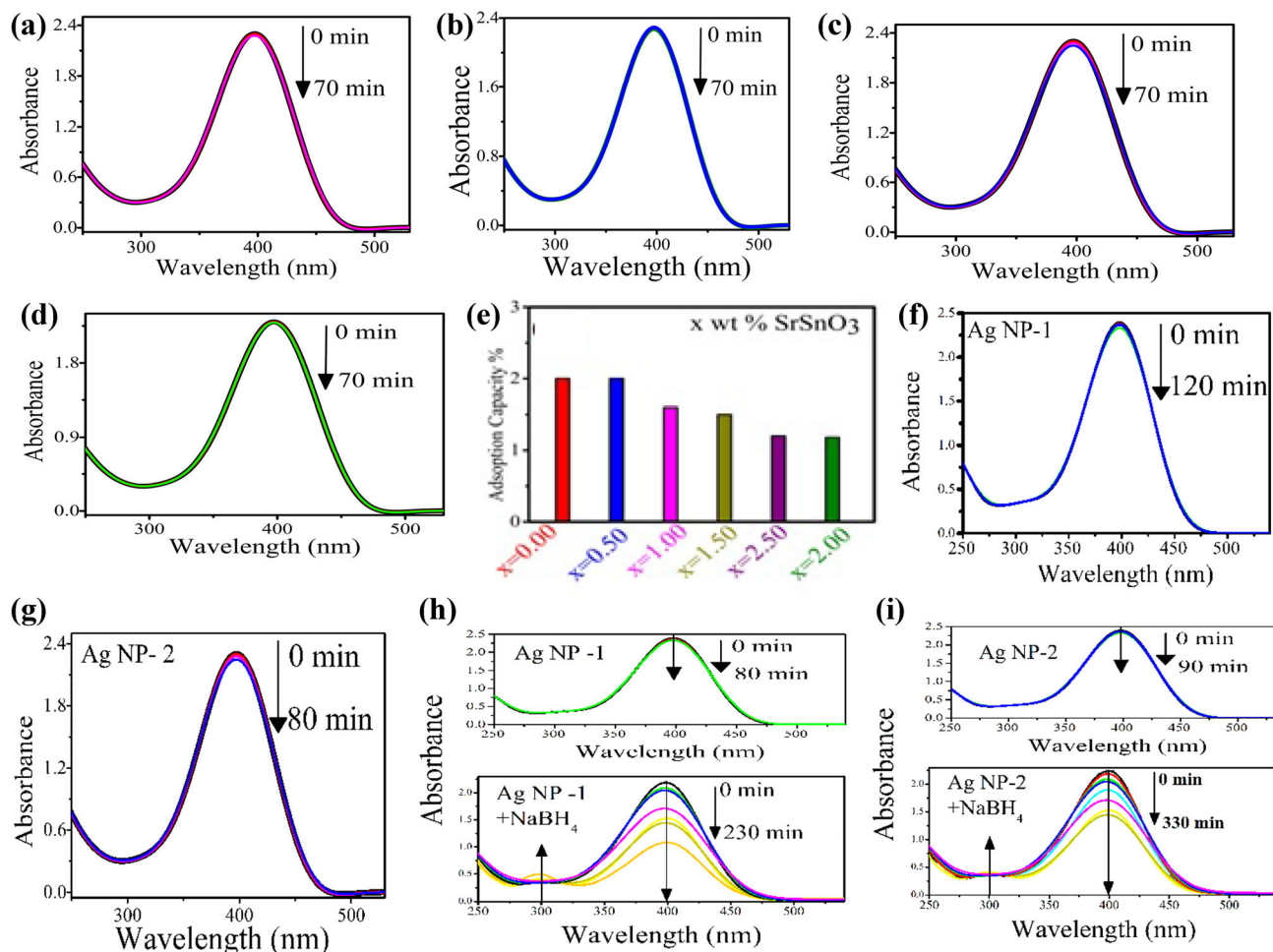
Fig. 4 Absorption spectra of 4-NP in the presence of NaBH$_4$ in dark (**a**) and under visible light illumination (**b**). Absorption spectra of 4-NP in the presence SrSnO$_3$ in dark, **c** and under visible light illumination (**d**). The adsorption % of prepared photocatalysts for 4-NP under different reaction conditions (**e**), and **f**, **g** absorption spectra of 4-NP in dark in the presence Ag NP-1 (**f**) and Ag NP-2 (**g**). Absorption spectra of 4-NP in the dark and under visible light in the presence Ag NP-1/NaBH **h** and Ag NP-2/NaBH **i**
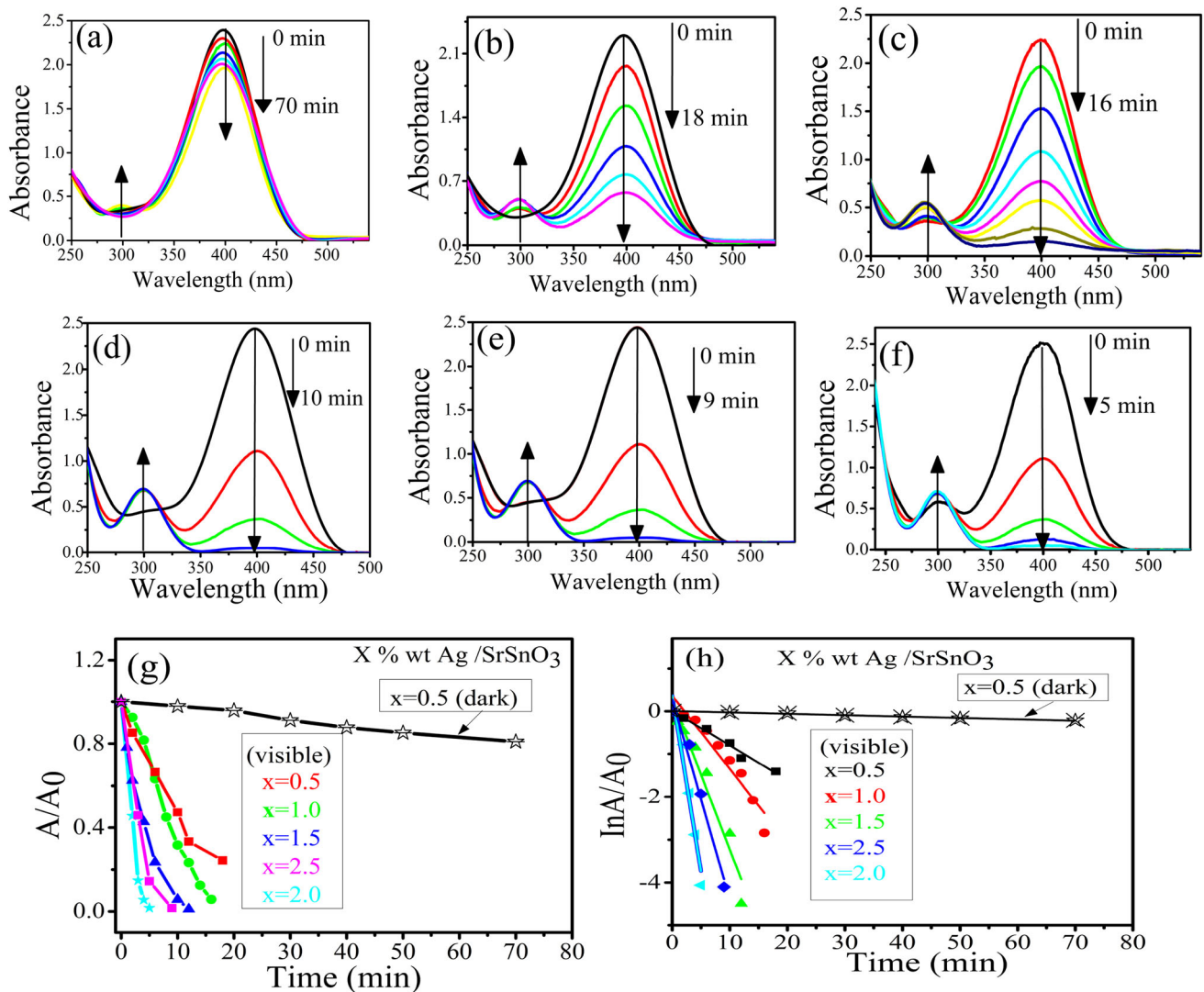
Fig. 5 Absorption spectra of 4-NP reduction using 0.5 wt% Ag/SrSnO$_3$ in dark, NaBH$_4$ (**a**) as well as under visible light illumination with Ag NPs content: **b** 0.5 wt%, **c** 0.10 wt%, **d** 1.5 wt%, **e** 2.5 wt%, **f** 2.0 wt% Ag/SrSnO$_3$. Plots of A/A$_0$ (**g**) and ln(A/A$_0$) (**h**) versus reaction time for the catalytic reduction of 4-NP to 4-AP using (0–2.5) Ag/SrSnO$_3$ with different conditions

nitrophenol, resulting in a reduction in reduction efficiencies [33].

Figure 5a shows the UV–Vis absorption spectra of blank in the dark using 0.5 wt% of Ag/SrSnO$_3$ and NaBH$_4$. Figure 5b, f display the gradual decrease in UV–Vis absorption spectra for 4-NP as a function of visible light illumination times in the presence of Ag/SrSnO$_3$ catalysts and NaBH$_4$ with different doping contents of Ag NPs. A new band around 300 nm was appeared due to formation of 4-aminophenol [36]. By increasing the loading content of Ag NPs, the photocatalytic activity of the Ag/SrSnO$_3$ increase. The higher photocatalytic reduction activity (98.2%) of 4-NP was observed within 5 min in the case of 2.0 wt

Ag/SrSnO$_3$ photocatalyst compared with AgNP-1, 2 only.

The rate constant of the reaction can be evaluated by the pseudo first-order kinetics according to the following Eq. (2) [37]:

$$\ln\left(\frac{A}{A_o}\right) = -k_{app}t \tag{2}$$

where A_o and A are the absorption intensity before illumination and at different times of illumination, respectively. k_{app} is an apparent rate constant. The relationships between ln (A/A$_o$) against t over Ag/SrSnO$_3$ catalysts are shown in Fig. 5g and h. The photocatalytic reduction of 4-NP follows the pseudo

Table 3 Kinetic parameters for the photocatalytic activity of different photocatalysts for reduction of 4-NP

Photocatalysts	Rate (k) min^{-1}	Reaction time (min)
0.5% Ag/SrSnO$_3$ (dark)	0.017	70
0.5% Ag/SrSnO$_3$ (light)	0.035	18
1.0% Ag/SrSnO$_3$ (light)	0.047	16
1.5% Ag/SrSnO$_3$ (light)	0.082	10
2.0% Ag/SrSnO$_3$ (light)	0.171	5.0
2.5% Ag/SrSnO$_3$ (light)	0.082	11

first-order kinetics. The degradation kinetic parameters of Ag/SrSnO$_3$ catalysts are summarized in Table 3. The rate constant values increase with increasing Ag NPs content, until reaches maximum at 2 wt% of Ag NPs and then decrease after adding 2.5 wt%. Compared to other reported candidates (Table 4), the as-prepared Ag-doped SrSnO$_3$ photocatalyst exhibit relatively higher photocatalytic reduction rate, suggesting that the prepared photocatalyst is promising material for water treatment.

The measured pH$_{IEP}$ value of 2.0% Ag/SrSnO$_3$ is 4.2, which is lower than the pk$_a$ value of 7.2 for 4-NP [38]. This indicates that under neutral condition (pH = 7.0), the surface of 2.0% Ag/SrSnO$_3$ and 4-NP have a negative charge, which means that in dark, the adsorption factor has less effect on the reaction rate (Figs. 3e, 4e and Table 3) [36, 39–42]. Also, the hydrolysis rate of borohydride ions increases by decreasing the pH of the medium [43, 44]. However, the measured rate of reaction for blank experiment without 2.0% Ag/SrSnO$_3$ photocatalyst, is very low, which enhances significantly in the presence of 2.0% Ag/SrSnO$_3$ and NaBH$_4$ in visible light.

### 3.2.2 Photocatalytic degradation of methylene blue

The photodegradation efficiency of MB dye was studied using Ag/SrSnO$_3$/H$_2$O$_2$ photocatalyst. The change in UV–Vis absorption maximum at λ_{max} = 664 nm was employed to monitor the entire photodegradation process. Also, the effect of H$_2$O$_2$ addition on the photocatalytic degradation of MB dye was also investigated in dark and under visible light illumination, as shown in Fig. 6a, b. Remarkable very slow degradation of the dye was observed in the dark under visible light illumination. However, a small change in the absorption spectrum of MB was observed in presence of SrSnO$_3$ and 0.5 wt% Ag/SrSnO$_3$ in dark, Fig. 6c, d.

Moreover, the SrSnO$_3$ shows a small change in the absorption spectrum of MB under visible light illumination, Fig. 6e. This is due to the high bandgap energy of SrSnO$_3$ (3.8 eV), which activated with UV illumination more than visible light as shown in Fig. 6e, weak adsorption of MB was observed on the photocatalyst surface under different condition, as shown in Fig. 6f. Furthermore, weak adsorption was observed in the dark, where oxidation of MB under visible light was observed in the presence and absence of Ag NP 1, 2. (g–i). As a positive-charged cationic dye, MB can reduce the adsorption of low-value negatively charged Ag NP-1 and AgNP-2 on the surface, lowering degradation efficiencies [33]. It is well known that MB can be present in aqueous solution as the cationic species (MB$^+$) and undissociated molecules (MB^0). Also, the (MB$^+$) is only species present at pH > 6 [45]. At experimental pH condition, both forms are present. Although, the photocatalyst carrying a negative charge (IEP at pH = 4.2), the presence of undissociated molecules (MB^0) decreases the adsorption efficiency of MB on the photocatalyst surface. Ag/SrSnO$_3$ shows higher decolorization efficiency under visible light illumination, Fig. 7a. This due to presence of Ag NP lowering the bandgap energy and acts as a sensitizer for SrSnO$_3$. To accelerate the reaction rate, H$_2$O$_2$ was used in combination with Ag/SrSnO$_3$. Figure 7b shows that the addition of H$_2$O$_2$ enhances the decolorization efficiency of 0.5 wt% Ag/SrSnO$_3$ under visible illumination. Figure 7b–f show that less

Table 4 Comparison of the characteristic data from literature

| Photocatalyst	Time (min)	Decomposition (%)	Ref.
6%Au/g-C$_3$N$_4$	8	100	[39]
5%Ag (10 nm)/g-C$_3$N$_4$	210	100	[40]
MIL-125/Ag/g-C$_3$N$_4$	30	82	[41]
1.5 Ag/g-C$_3$N$_4$/V$_2$O$_5$	8	100	[42]
2% Ag/SrSnO$_3$	5	98.2	This work
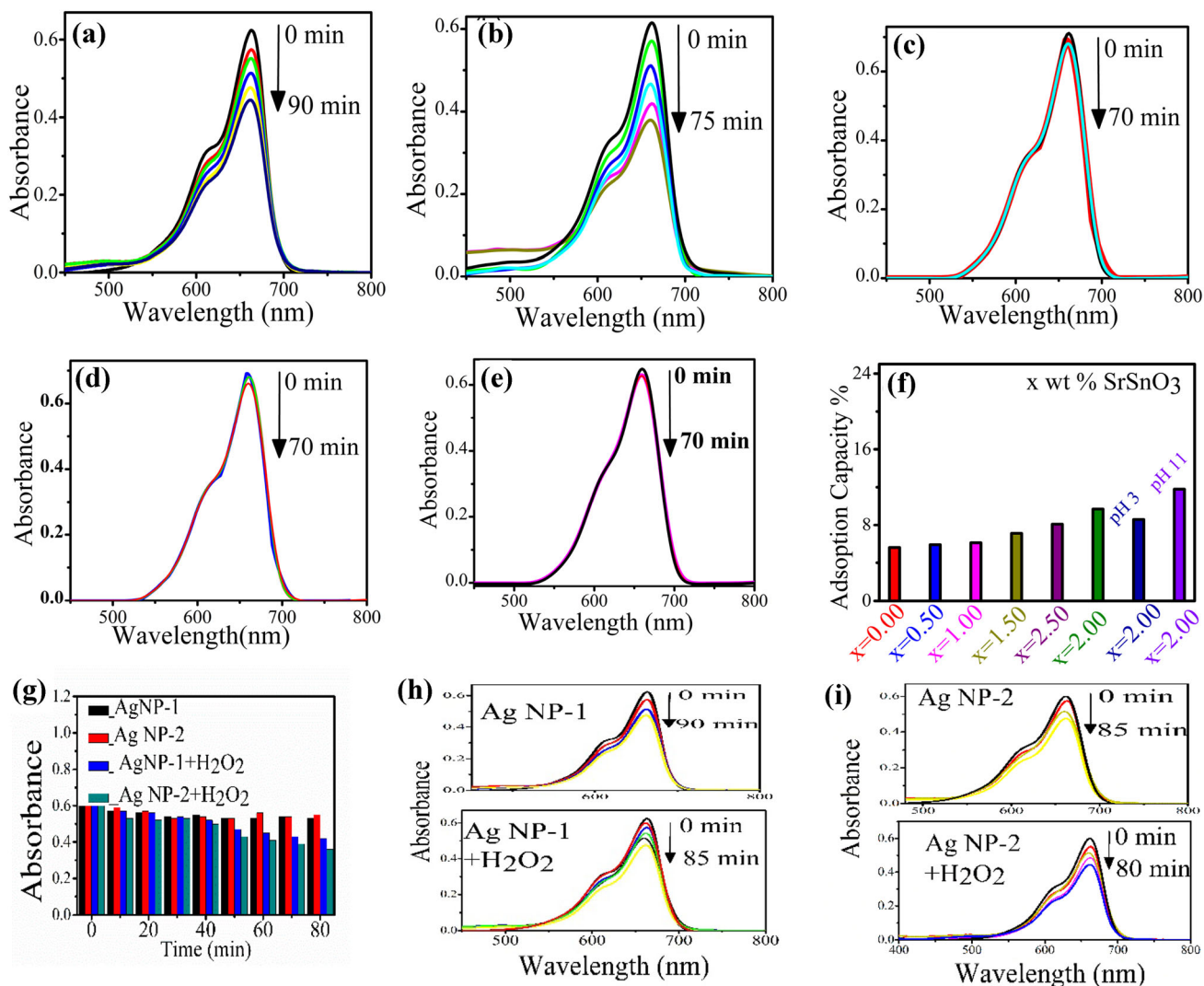
Fig. 6 Absorption spectra of MB in the presence of H_2O_2 (0.08 mol) in dark (**a**), under visible light illumination (**b**). Absorption spectra of MB in the presence $SrSnO_3$ (**c**). Ag/$SrSnO_3$ (**d**). Absorption spectra of MB in the presence $SrSnO_3$ under visible light illumination, **e**. The adsorption % of prepared photocatalysts for MB under different reaction conditions (**f**), Absorption of MB with time in the presence Ag NP-1, Ag NP-2, H_2O_2, absence H_2O_2 in dark (**g**), and under visible light (**h**, **i**)

time was needed for complete disappearance of the intense blue color (MB) to colorless leucomethylene blue (LMB) by increasing concentration of loading Ag NPs until reached to optimum concentration 2 wt%. The Ag NPs concentrations of 0.5, 1.0, 1.5, 2.0 and 2.5 produce complete decolorization within 70, 64, 60, 40 and 50 min, respectively. The linear plot of (A/A_0) vs time (t) are shown in Fig. 7g. The degradation rate constants were determined from the linear plot of $\ln(A_t/A_0)$ vs time (t), (Fig. 7h) and the results are summarized in Table 5. All experiments were performed at pH = 5.5 using 0.08 mol of H_2O_2 in the presence of 20 mg (0–2.5) wt% of Ag/$SrSnO_3$.

Figure 8a–c show the effect of pH on the photocatalytic activity of 2.0 wt% Ag NPs content of Ag/$SrSnO_3$ for degradation of MB in the presence of H_2O_2. As shown in Table 5, the decolorization of MB using Ag/$SrSnO_3$ is depending on pH value. Complete decolorization occurs within 26 min at pH = 11. The values of the decolorization rate constants were 0.025, 0.058 and 0.107 at pH values of 3.0, 6.0 and 11, respectively, Fig. 8d, e and in Table 5. The gradual increase in the photocatalytic activity was mainly due to the predominant cationic MB^+ species at pH > 6. Also, the negative charge of the surface of Ag/$SrSnO_3$ increases by increasing the pH of the solution. The
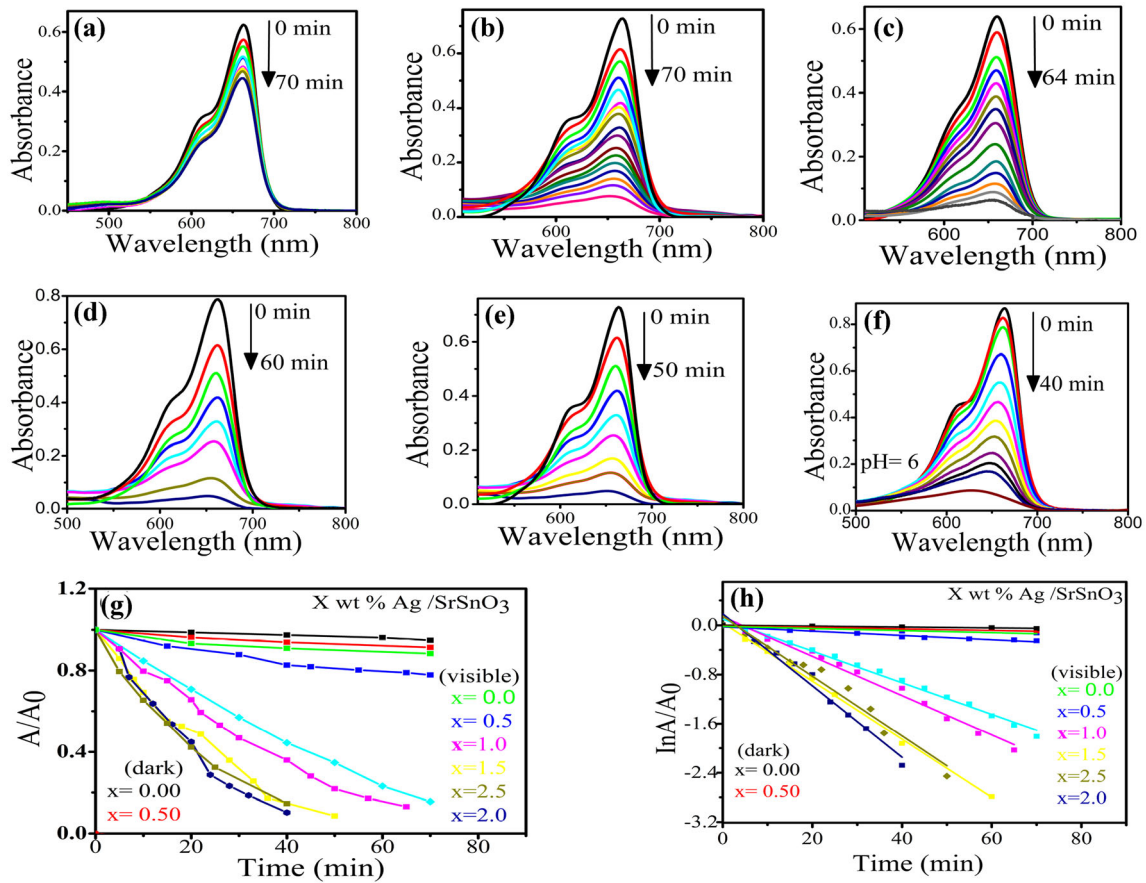
Fig. 7 Absorption spectra of MB in the presence of Ag/SrSnO₃ under visible light illumination: (**a**), in the absence of H₂O₂ and 0.5 wt% Ag NPs content, (**b**) presence of H₂O₂/0.5 wt% Ag NPs content, (**c**) presence H₂O₂/0.10% wt Ag NPs content, (**d**) presence of H₂O₂/1.5 wt% Ag NPs content, (**e**) presence of H₂O₂/2.5 wt% Ag NPs content and (**f**) presence of ₂O₂/2.0 wt% Ag. Plots of (**g**) A/A_0 and (**h**) $\ln(A/A_0)$ versus reaction time for the photocatalytic degradation of MB.

Table 5 Kinetic parameters for the MB catalytic degradation activity using different photocatalysts under dark and light conditions

Photocatalysts	Rate (k) min^{-1}	Reaction time (min)
SrSnO₃ (dark)	0.0090	70
SrSnO₃ (light)	0.012	70
0.5% Ag/SrSnO₃ (dark)	0.016	70
0.5% Ag/SrSnO₃ (light)	0.017	70
0.5 Ag/SrSnO₃/H₂O₂ (light)	0.026	70
1.0 Ag/SrSnO₃/H₂O₂ (light)	0.032	64
1.5 Ag/SrSnO₃/H₂O₂ (light)	0.047	60
2.0 Ag/SrSnO₃/H₂O₂ (light) pH = 6	0.058	40
2.0 Ag/SrSnO₃/H₂O₂ (light) pH = 3	0.025	70
2.0 Ag/SrSnO₃/H₂O₂ (light) pH = 11	0.107	26

electrostatic attraction between the cationic form of MB and the negative photocatalyst surface improve the adsorption ability and consequently the photocatalytic activity.

Additionally, the photodegradation efficiency of MB was investigated using the highly active nanoparticles (2.0% Ag/SrSnO₃ in the presence of H₂O₂) using total organic carbon before degradation (TOC₀) and after degradation (TOC) measurement. The obtained results show that the TOC value reduced from 100 mg/l (TOC₀) to 13 mg/l (TOC) after 1 h of visible light illumination. This implies

Fig. 8 (a), (b) and (c) Photocatalytic activity for MB decolorization by 2 wt% Ag/SrSnO₃ in the presence of H_2O_2 at different pH values, Plots of (d) A/A_0 and e $\ln(A/A_0)$ versus reaction time for the photocatalytic oxidation MB under visible light illumination using 2.0% Ag/SrSnO₃ at different pH value
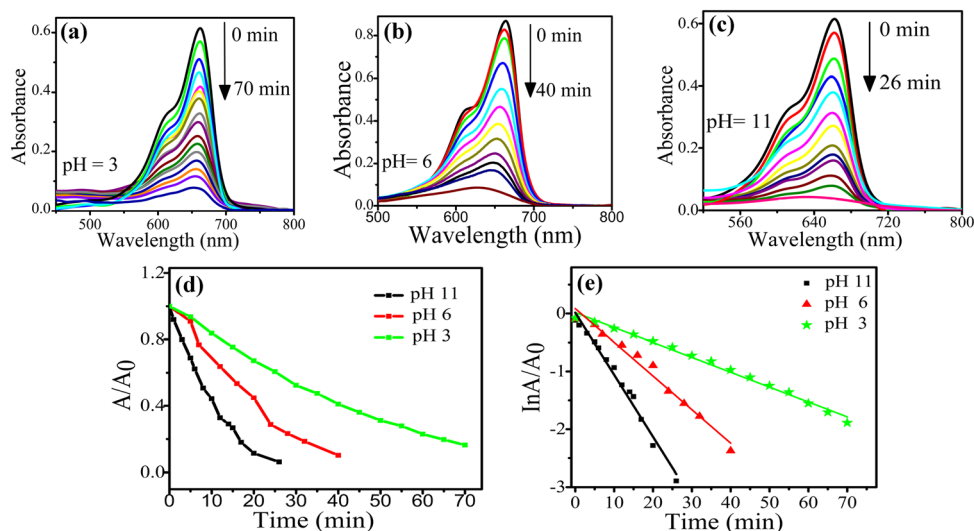
that 87% of the sample was completely decomposed after 1 h (Fig. 9a).

SrSnO₃ absorption was difficult in the presence of direct light as a result of its large bandgap (3.8 eV), which greatly diminished its usage as a photocatalyst under visible light, Scheme 1 To improve the photocatalytic process, plasmonic noble metals such as Ag NPs were doped SrSnO₃to increase visible light absorption. Degradation of organic pollutants is dominated by photo generated electron – hole pairs. As a result, the method was used to calculate the Conduction Band (CB) and VB (Valence Band) potentials for catalysts by the following Eqs. (3,4) to study the photocatalytic process [46],

$$E_{CB} = \chi - E^e - 0.5E_g \tag{3}$$

$$E_{VB} = E_{CB} + E_g \tag{4}$$

The potential energies of the conduction and valence bands are E_{CB} and E_{VB}, respectively, while E^e is the energy of free electrons against a normal hydrogen electrode (4.5 eV). The resulting electronegativity of different individual semiconductors is given by the following Eq. (5) [47]

$$\chi = [\chi(A)^a \chi(B)^b \chi(C)^c]^{1/(a+b+c)} \tag{5}$$

where a, b, and c are the number of atoms in semiconductors. The measured CB and VB potentials of SrSnO₃ were − 0.996 and 2.81 eV, respectively. As shown in Scheme 1, the surface plasmon resonance (SPR) phenomenon occurs on the surface Ag NPs under irradiation of Ag/SrSnO₃ with visible light. This leads to movement of electrons on surface Ag NPs to the other side. Then the interfacial electron transfer from

flow from Ag NPs to CB of SrSnO₃, producing a positive charge on the Ag NPs [45]. SrSnO₃ was responsible for trapping electrons, charge separation and slow down the rate of recombination photogenerated charge carriers [12, 13, 48]. However, the reaction of H_2O_2 with electrons on the CB of SrSnO₃ produces highly reactive hydroxyl radicals that oxidize MB. SrSnO₃'s CB position has more negative than the possibility for oxidize MB decrease (− 0.33 eV vs NHE). At the same time, h^+ on surface Ag NPs interacted immediately with H_2O to produce OH^- then MB was oxidized (MB-OX), creating water and carbon dioxide that is good for the environment [36, 49, 50].

The proposed mechanism for 4-NP reduction using the Ag/SrSnO₃ catalyst in the presence of NaBH₄ is shown in Scheme 2. The experimental results show that the reduction rate in the presence of NaBH₄ alone is very slow but enhanced significantly in the presence of Ag NPs on the surface of photocatalyst.

Under irradiation of Ag/SrSnO₃ with Visible light, the surface plasmon resonance (SPR) phenomenon occurs on the surface of Ag NPs. This leads to movement of electrons on surface Ag NPs to the other side. Then the interfacial electron transfer from Ag NPs to SrSnO₃ induces a positive charge on the Ag NPs (Scheme 2). Consequently, this enhances the adsorption ability of BH_4^- and the 4-NP onto the surface of positively charged Ag NPs compared with Ag NP only. Then the reaction starts by hydrolysis of the borohydride ions. The BO_2^- is one of the borohydride ion hydrolysis products. BO_2^- deprotonates 4-nitrophenols form 4-nitrophenolate ions (4-NPat)

Fig. 9 Plots of TOC/TOC$_0$ a versus reaction time for degradation of MB (**a**). Trapping agents' effect on the degradation of MB, 4-NPs by Ag/SrSnO$_3$ under visible light (**b**), stability of Ag/SrSnO$_3$ under visible light irradiation for degradation MB (**c**) and 4-NP (**d**)
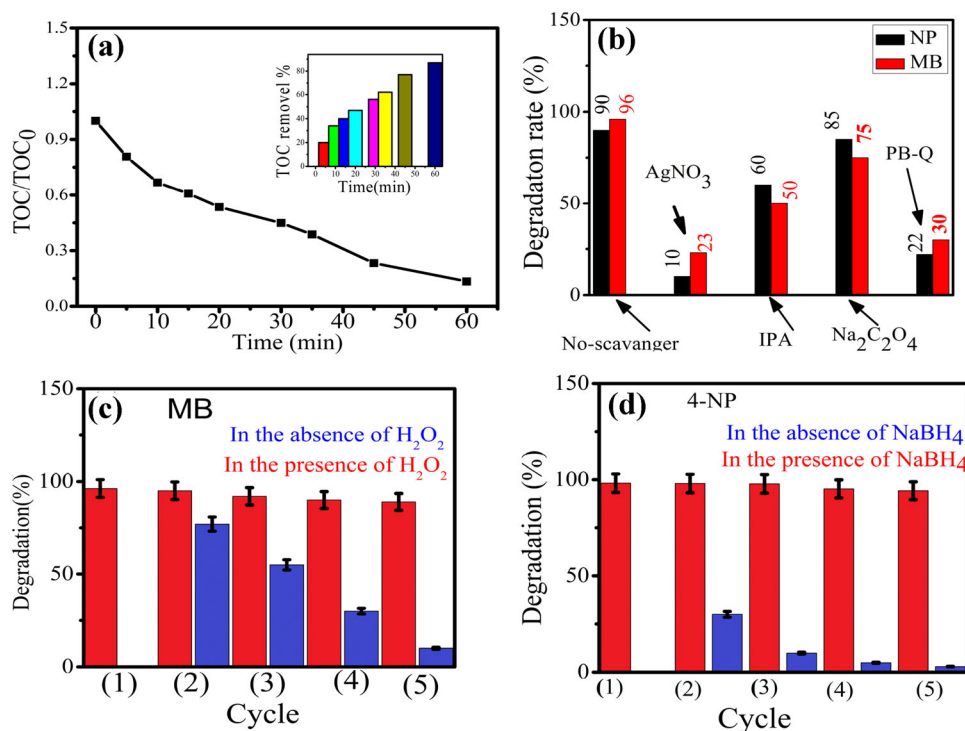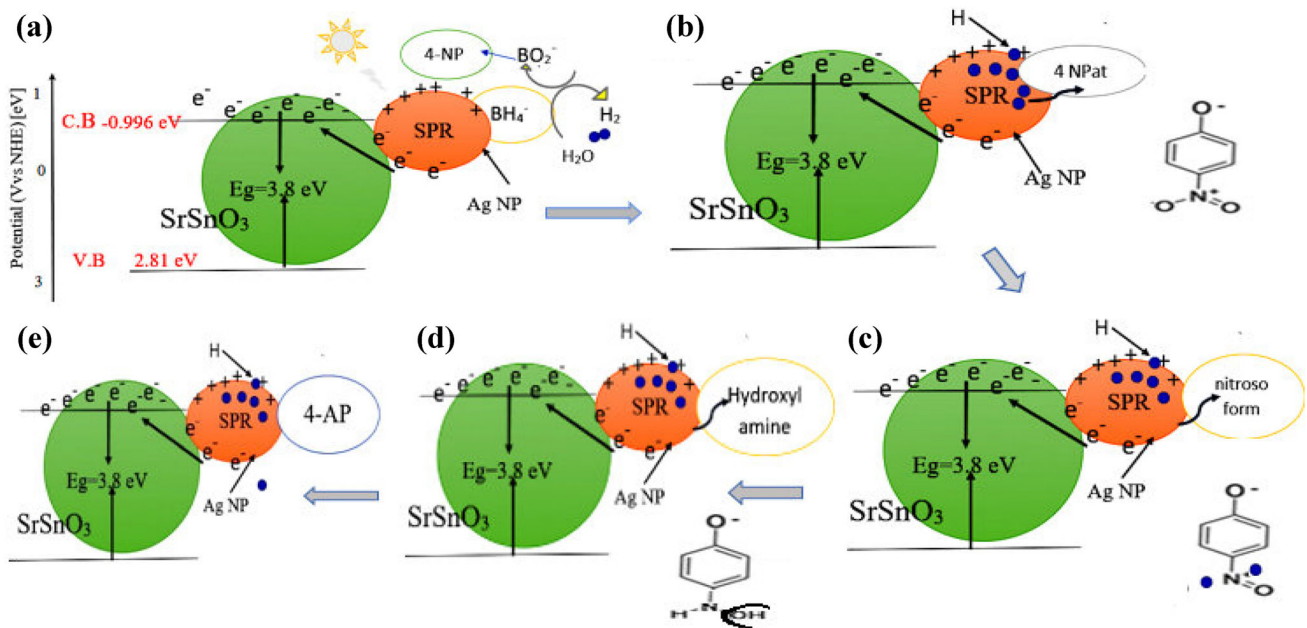

Scheme 1 Possible photo catalytic process for the degradation of MB and in the presence of Ag/SrSnO$_3$ and H$_2$O$_2$
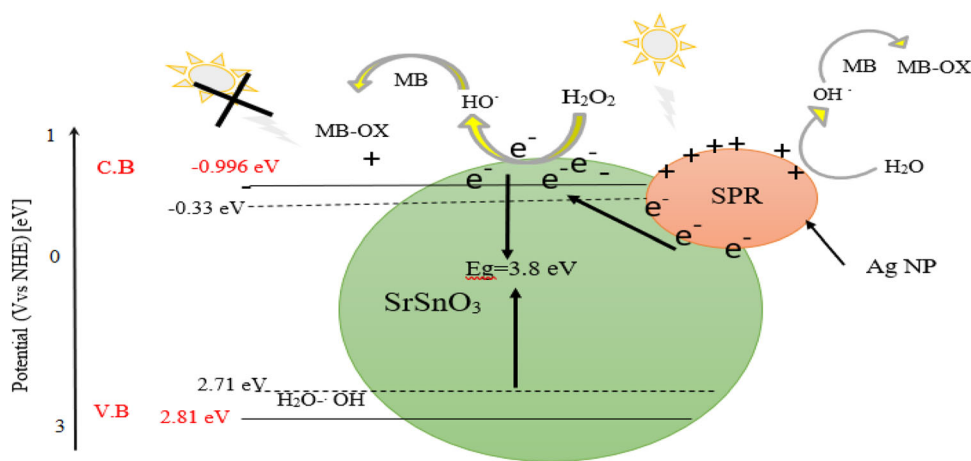
on the photocatalyst surface (Scheme 2b) [51]. Also, borohydride ions react with the Ag NPs and produce hydrogen gas as a source of an active hydrogen species on it (Ag–H). These hydrogen species are unstable and have a negative charge in the metal–hydrogen structure. As consequences, it can easily attack the positively charged nitrogen in the nitro group of nitrophenols to produce nitroso group (Scheme 2c). This is followed by the reductive addition of two hydrogen atoms to form hydroxylamine (Scheme 2d). Finally, the hydroxylamine is further reduced to the 4-AP (Scheme 2e) [43, 52].

Figure 9b shows trapping experiment to confirm the suggested mechanism by addition of different scavengers. We utilized p-benzoquinone PBQ (0.1 mmol), isopropanol IPA (0.1 mol L^{-1}), silver nitrate AgNO$_3$ (0.1 mmol), and sodium oxalate Na$_2$C$_2$O$_4$ (0.1 mmol) as $\cdot$O$_2$, $\cdot$OH, electron, and h$^+$ scavengers, respectively. These results indicate that photogenerated electrons play a significant role in the removal of organic compound, while OH and h playing a secondary function.

From an economic point of view, the chemical stability of the photocatalyst is the main issue. Therefore, we performed the stability of Ag/SrSnO$_3$

Scheme 2 Possible photo catalytic process for the degradation of 4-NP and in the presence of Ag/SrSnO$_3$ and NaBH$_4$

under five cycles of photocatalytic degradation of MB as shown in Fig. 9c, d. The five cycles degradation of MB and 4-NPs were performed under the same condition in the presence of H$_2$O$_2$ and NaBH$_4$. It is apparent that the degradation efficiency of Ag/SrSnO$_3$ was not significantly decreased after three-time photocatalytic cycles. The degradation efficiency of MB only decreases from 96.5 to 93.4% and reduction efficiency of 4-NPs decreased slightly from 98.2 to 95.5%. The decrease in the photocatalytic efficiency related to the decreasing of concentration Ag NPs. The ICP results showed a slight decrease of Ag NPs concentration from 2.0 to 1.88%) [35]. Whereas After 1 cycle the degradation efficiency of MB and reduction efficiency 4-NPs by Ag/SrSnO$_3$ in absence H$_2$O$_2$ and NaBH$_4$ decreased from 96.5–10% to 98.2–5%, respectively indicating H$_2$O$_2$ and NaBH$_4$ has synergistic effect with Ag/SrSnO$_3$.

4 Conclusions

Silver-doped perovskite strontium stannate with different wt% (Ag/SrSnO$_3$) was prepared by hydrothermal method followed by ultrasonic treatment. The effect of hydrothermal time, CTAB and Ag NPs loading were studied. All samples exhibited a well-defined crystalline cubic phase of SrSnO$_3$ with rod like morphology. CTAB inhibits the crystal growth of SrSnO$_3$.

The UV–Vis absorption measurements confirm the formation of Ag doped on the surface of SrSnO$_3$ via appearance of high intense surface plasmon resonance absorption band of Ag NP. The high ς-potential value of Ag/SrSnO$_3$ suspension (− 39 mV) refers to its electrical stability. The prepared photocatalysts were applied for the reduction of 4-nitrophenol (4-NP) and degradation of MB under visible light. The obtained results show that 2 wt% of Ag/SrSnO$_3$ is highly active sample. 2.0 wt% Ag/SrSnO$_3$ photocatalyst reduces 4-NP with 100% conversion within 5 min of reaction time. Also, 87% of the MB sample was mineralized after 1 h of visible illumination using 2.0% Ag/SrSnO$_3$ in the presence of H$_2$O$_2$.

Author contributions

ZG: experiments, analyzed data and original draft, RK and HM: data acquisition, conceptualization, reviewing. MS and HH: supervision, conceptualization, reviewing, ME-K: supervision, conceptualization, editing & review, and funding acquisition.

Funding

Data availability

All data generated or analyzed during this study are included in this published article.

Declarations

Conflict of interest The authors have no conflict of interest to declare that are relevant to the content of this article.

Ethical approval Not applicable.

References

1. J. Dou, D. Gan, Q. Huang, M. Liu, J. Chen, F. Deng, X. Zhu, Y. Wen, X. Zhang, Y. Wei, Functionalization of carbon nanotubes with chitosan based on MALI multicomponent reaction for Cu^{2+} removal. Int. J. Biol. Macromol. **36**, 476–485 (2019)

2. Q. Huang, M. Liu, J. Zhao, J. Chen, G. Zeng, H. Huang, J. Tian, Y. Wen, X. Zhang, Y. Wei, Facile preparation of polyethylenimine-tannins doped SiO_2 hybrid materials for Cu^{2+} removal. Appl. Surf. Sci. **427**, 535–544 (2018)

3. Y. Liu, H. Huang, D. Gan, L. Guo, M. Liu, J. Chen, F. Deng, N. Zhou, X. Zhang, Y. Wei, A facile strategy for preparation of magnetic graphene oxide composites and their potential for environmental adsorption. Ceram. Int. **44**, 18571–18577 (2018)

4. T. Welderfael, M. Pattabi, R.M. Pattabi, Photocatalytic activity of Ag-N co-doped ZnO nanorods under visible and solar light irradiations for MB degradation. J. Water Process. Eng. **14**, 117–123 (2016)

5. R. El-Shabasy, N. Yosri, H. El-Seedi, K. Shoueir, M. El-Kemary, A green synthetic approach using chili plant supported $Ag/Ag_2O@P25$ heterostructure with enhanced photocatalytic properties under solar irradiation. Optik **192**, 162943 (2019)

6. A. Mezni, N.B. Saber, M.M. Ibrahim, M. El-Kemary, A. Aldalbahi, P. Feng, L.S. Smiri, T. Altalhi, Facile synthesis of highly thermally stable TiO_2 photocatalysts. New J. Chem. **41**, 5021–5027 (2017)

7. C.W. Lee, D.W. Kim, I.S. Cho, S. Park, S.S. Shin, S.W. Seo, K.S. Hong, Simple synthesis and characterization of $SrSnO_3$ nanoparticles with enhanced photocatalytic activity. Int. J. Hydrog. Energy **37**, 10557–10563 (2012)

8. Z. Ghubish, R. Kamal, H.R. Mahmoud, M. Saif, H. Hafez, M. El-Kemary, Novel fluorescent nano-sensor based on amino-functionalization of Eu^{3+}: $SrSnO_3$ for copper ion detection in food and real drink water samples. RSC Adv. **11**(30), 18552–18564 (2021)

9. I.A. de Sousa Filho, I.T. Weber, $SrSnO_3/g-C_3N_4$ dry phase sunlight photocatalysis. J. Photochem. Photobiol. A **412**, 113255 (2021)

10. H. Mizoguchi, H.W. Eng, P.M. Woodward, Probing the electronic structures of ternary perovskite and pyrochlore oxides containing Sn^{4+} or Sb^{5+}. Inorg. Chem. **43**, 1667–1680 (2004)

11. M.F. Abdelbar, M. El-Kemary, N. Fukata, Downshifting of highly energetic photons and energy transfer by Mn-doped perovskite $CsPbCl_3$ nanocrystals in hybrid organic/silicon nanostructured solar cells. Nano Energy **77**, 105163 (2020)

12. L.G. Devi, R. Kavitha, A review on plasmonic metal- TiO_2 composite for generation, trapping, storing and dynamic vectorial transfer of photogenerated electrons across the Schottky junction in a photocatalytic system. Appl. Surf. Sci. **360**, 601–622 (2016)

13. H. Gerischer, A. Heller, The role of oxygen in photooxidation of organic molecules on semiconductor particles. J. Phys. Chem. **95**, 5261–5267 (1991)

14. M.A. Subhan, T.P. Rifat, P.C. Saha, M.M. Alam, A.M. Asiri, T. Raihan, A.K. Azad, W. Ghann, J. Uddin, M.M. Rahman, Photocatalytic, anti-bacterial performance and development of 2, 4-diaminophenylhydrazine chemical sensor probe based

on ternary doped Ag· SrSnO$_3$ nanorods. New J. Chem. **45**, 1634–1650 (2021)

15. P. Junploy, T. Thongtem, S. Thongtem, A. Phuruangrat, Decolorization of methylene blue by Ag/SrSnO$_3$ composites under ultraviolet radiation. J. Nanomater. **67**, 2014 (2014)

16. G. Venkatesh, M. Geerthana, S. Prabhu, R. Ramesh, K.M. Prabu, Enhanced photocatalytic activity of reduced graphene oxide/SrSnO$_3$ nanocomposite for aqueous organic pollutant degradation. Optik **206**, 164055 (2020)

17. I.A.S. Filho, I.T. Weber, SrSnO$_3$/g-C$_3$N$_4$ dry phase sunlight photocatalysis. J. Photochem. Photobiol. A **1**, 113255 (2021)

18. L. Mulfinger, S.D. Solomon, M. Bahadory, A.V. Jeyarajasingam, S.A. Rutkowsky, C. Boritz, Synthesis and study of silver nanoparticles. J. Chem. Educ. **84**, 322 (2007)

19. A. Mezni, M.M. Ibrahim, M. El-Kemary, A.A. Shaltout, N.Y. Mostafa, J. Ryl, T. Kumeria, T. Altahi, M.A. Amin, Cathodically activated Au/TiO$_2$ nanocomposite synthesized by a new facile solvothermal method: an efficient electrocatalyst with Pt-like activity for hydrogen generation. Electrochim. Acta **290**(10), 404–418 (2018)

20. D. Yang, C. Zhang, L. Dong, X. Hou, W. Zheng, J. Xu, H. Ma, Synthesis and properties of SrSn(OH)$_6$ nanorods and their flame retardancy and smoke suppression effects on epoxy resin. J. Coat. Technol. Res. **16**, 1715–1725 (2019)

21. C. Li, Y. Zhu, S. Fang, H. Wang, Y. Gui, L. Bi, R. Chen, Preparation and characterization of SrSnO$_3$ nanorods. J. Phys. Chem. Solids **72**(7), 869–874 (2011)

22. D.N. Srivastava, S. Chappel, O. Palchik, A. Zaban, A. Gedanken, Sonochemical synthesis of mesoporous tin oxide. Langmuir **18**, 4160 (2002)

23. C.V. Squez, M. Luisa, O.A. Campero, J.M. Esparza, F. Rojas, Surfactantless synthesis and textural properties of self-assembled mesoporous SnO$_2$. Nanotechnology **17**, 3347 (2006)

24. C.V. Squez, F. Rojas, M.L. Ojeda, A.A. Ortiz, Campero, structure and texture of self-assembled nanoporous SnO$_2$. Nanotechnology **16**, 127 (2005)

25. D. Chen, J. Ye, SrSnO$_3$ nanostructures: synthesis, characterization, and photocatalytic properties. Chem. Mater. **19**, 4585–4591 (2007)

26. P. Junploy, S. Thongtem, T. Thongtem, Photoabsorption and photocatalysis of SrSnO$_3$ produced by a cyclic microwave radiation. Superlattices Microstruct. **57**, 1–10 (2013)

27. L.S. Daniel, H. Nagai, M. Sato, Absorption spectra and photocurrent densities of Ag nanoparticle/TiO$_2$ composite thin films with various amounts of Ag. J. Mater. Sci. **48**, 7162–7170 (2013)

28. X. Yin, W. Que, D. Fei, F. Shen, Q. Guo, Ag nanoparticle/ZnO nanorods nanocomposites derived by a seed-mediated method and their photocatalytic properties. J. Alloys Compd. **524**, 13–21 (2012)

29. D.L. Wood, J. Tauc, Weak absorption tails in amorphous semiconductors. J. Phys. Rev. **5**, 3144–3151 (1972)

30. W.F. Zhang, J. Tang, J. Ye, Photoluminescence and photocatalytic properties of SrSnO$_3$ perovskite. Chem. Phys. Lett. **418**, 174–178 (2006)

31. Z. Ghubish, M. Saif, H. Hafez, H. Mahmoud, R. Kamal, M. El-Kemary, Novel red photoluminescence sensor based on Europium ion doped calcium hydroxy stannate CaSn (OH)$_6$: Eu^{3+} for latent fingerprint detection. J. Mol. Struct. **1207**, 127840 (2020)

32. Y. Hong, Y. Jiang, C. Li, W. Fan, X. Yan, M. Yan, W. Shi, In-situ synthesis of direct solid-state Z-scheme V$_2$O$_5$/g-C$_3$N$_4$ heterojunctions with enhanced visible light efficiency in photocatalytic degradation of pollutants. Appl. Catal. B **180**, 663 (2016)

33. C. Yang, W. Dong, G. Cui, Y. Zhao, X. Shi, X. Xia, W. Wang, Highly-efficient photocatalytic degradation of methylene blue by PoPD-modified TiO$_2$ nanocomposites due to photosensitization-synergetic effect of TiO$_2$ with PoPD. Sci. Rep. **7**, 1–12 (2017)

34. N.T. Baliah, P. Muthulakshmi, S.L. Priyatharsini, Synthesis and characterization of onion mediated silver doped zinc oxide nanoparticles. J. Sci. Res. Sci. Eng. Technol. **4**, 111–120 (2018)

35. H.P. Jing, C.C. Wang, Y.W. Zhang, P. Wang, R. Li, Photocatalytic degradation of methylene blue in *ZIF-8*. RSC Adv. **4**, 54454 (2014)

36. H.S. El-Sheshtawy, Z. Ghubish, K.R. Shouir, M. El-Kemary, Activated H$_2$O$_2$ on Ag/SiO$_2$–SrWO$_4$ surface for enhanced dark and visible-light removal of methylene blue and p-nitrophenol. J. Alloys Compd. **842**, 155848 (2020)

37. S. Khezrianjoo, H.D. Revanasiddappa, Langmuir-Hinshelwood kinetic expression for the photocatalytic degradation of Metanil Yellow aqueous solutions by ZnO catalyst. Chem. Sci. J. **85**, 1–7 (2012)

38. F.H. Lin, R. Doong, Highly efficient reduction of 4-nitrophenol by heterostructured gold-magnetite nano catalysts. Appl. Catal. A **486**, 32–41 (2014)

39. Y. Fu, T. Huang, B. Jia, J. Zhu, X. Wang, Reduction of nitrophenols to aminophenols under concerted catalysis by Au/g-C$_3$N$_4$ contact system. Appl. Catal. B **202**, 430–437 (2017)

40. Y. Yang, Y. Guo, F. Liu, X. Yuan, Y. Guo, S. Zhang, W. Guo, M. Huo, Preparation and enhanced visible-light photocatalytic activity of silver deposited graphitic carbon nitride plasmonic photocatalyst. Appl. Catal. B **142–143**, 828–837 (2013)

41. Z. Yang, X. Xu, X. Liang, C. Lei, Y. Cui, W. Wu, Y. Yang, Z. Zhang, Z. Lei, Construction of heterostructured MIL-125/Ag/g-C$_3$N$_4$ nanocomposite as an efficient bifunctional visible light photocatalyst for the organic oxidation and reduction reactions. Appl. Catal. B **205**, 42–54 (2017)

42. H.S. El-Sheshtawy, H.M. El-Hosainy, K.R. Shoueir, I.M. El-Mehasseb, M. El-Kemary, Facile immobilization of Ag nanoparticles on g-C$_3$N$_4$/V$_2$O$_5$ surface for enhancement of post-illumination, catalytic, and photocatalytic activity removal of organic and inorganic pollutants. Appl. Surf. Sci. **467**, 268–276 (2019)

43. S.M. Sadeghzadeh, R. Zhiani, S. Emrani, The reduction of 4-nitrophenol and 2-nitroaniline by the incorporation of Ni@Pd MNPs into modified UiO-66-NH$_2$ metal–organic frameworks (MOFs) with tetrathia-azacyclopentadecane. New J. Chem. **42**, 988–994 (2018)

44. J.H. Lee, S.K. Hong, W.B. Ko, Reduction of 4-nitrophenol catalyzed by platinum nanoparticles embedded into carbon nanocolloids. Asian J. Chem. **23**, 2347–2350 (2011)

45. L. Zhang, C. Liang, H. Guo, C.-G. Niu, X.-F. Zhao, X.-J. Wen, G.-M. Zeng, Construction of a high-performance photocatalytic fuel cell (PFC) based on plasmonic silver modified Cr-BiOCl nanosheets for simultaneous electricity production and pollutant removal. Nanoscale **11**, 6662–6676 (2019)

46. Z. Lihong, X. Wang, Q. Nong, H. Lin, B. Teng, Y. Zhang, L. Zhao, T. Wu, Y. He, Enhanced visible-light photoactivity of g-C$_3$N$_4$ via Zn$_2$SnO$_4$ modification. Appl. Surf. Sci. **329**, 143–149 (2015)

47. Q. Yuan, L. Chen, M. Xiong, J. He, S.L. Luo, C.T. Au, S.F. Yin, Cu$_2$O/BiVO$_4$ heterostructures: synthesis and application in simultaneous photocatalytic oxidation of organic dyes and reduction of Cr (VI) under visible light. Chem. Eng. J. Chem. E **255**, 394–402 (2014)

48. P. Sanitnon, S. Chiarakorn, C. Chawengkijwanich, S. Chuangchote, T. Pongprayoon, Synergistic effects of zirconium and silver co-dopants in TiO$_2$ nanoparticles for photocatalytic degradation of an organic dye and antibacterial activity. J. Aust. Ceram. Soc. **56**, 579–590 (2020)

49. D. Chen, T. Li, Q. Chen, J. Gao, B. Fan, S.J. Li, L. Gao, hierarchically plasmonic photocatalysts of Ag/AgCl nanocrystals coupled with single-crystalline WO$_3$ nanoplates. Nanoscale **4**, 5431–5439 (2012)

50. H. Ye, S. Lu, Effect of hydrogen peroxide on the structure and photocatalytic activity of titania. Res. Chem. Interned. **41**, 139–149 (2015)

51. A.S. Hashimi, M.A.N.M. Nohan, S.X. Chin, S. Zakaria, C.H. Chia, Rapid catalytic reduction of 4-nitrophenol and clock reaction of methylene blue using copper nanowires. Nanomaterials **9**, 1–13 (2019)

52. G. Wu, X. Liu, P. Zhou, L. Wang, M. Hegazy, X. Huang, Y. Huang, A facile approach for the reduction of 4-nitrophenol and degradation of congo red using gold nanoparticles or laccase decorated hybrid inorganic nanoparticles/polymer-biomacromolecules vesicles. Mater. Sci. Eng. C **94**, 524–533 (2019)